Nonlocal plasmonic response of doped and optically pumped graphene, MoS_2, and black phosphorus

René Petersen,[1,2,*] Thomas Garm Pedersen,[1,2] and F. Javier García de Abajo[3,4,†]
[1]*Department of Physics and Nanotechnology, Aalborg University, DK-9220 Aalborg East, Denmark*
[2]*Center for Nanostructured Graphene (CNG), DK-9220 Aalborg East, Denmark*
[3]*ICFO-Institut de Ciencies Fotoniques, The Barcelona Institute of Science and Technology, 08860 Castelldefels (Barcelona), Spain*
[4]*ICREA-Institució Catalana de Recerca i Estudis Avançats, Passeig Lluís Companys, 23, 08010 Barcelona, Spain*
(Received 9 August 2017; revised manuscript received 26 October 2017; published 22 November 2017)

Plasmons in two-dimensional (2D) materials have emerged as a new source of physical phenomena and optoelectronic applications due in part to the relatively small number of charge carriers on which they are supported. Unlike conventional plasmonic materials, they possess a large Fermi wavelength, which can be comparable with the plasmon wavelength, thus leading to unusually strong nonlocal effects. Here, we study the optical response of a selection of 2D crystal layers (graphene, MoS_2, and black phosphorus) with inclusion of nonlocal and thermal effects. We extensively analyze their plasmon dispersion relations and focus on the Purcell factor for the decay of an optical emitter in close proximity to the material as a way to probe nonlocal and thermal effects, with emphasis placed on the interplay between temperature and doping. The results are based on tight-binding modeling of the electronic structure combined with the random-phase approximation response function in which the temperature enters through the Fermi-Dirac electronic occupation distribution. Our study provides a route map for the exploration and exploitation of the ultrafast optical response of 2D materials.

DOI: 10.1103/PhysRevB.96.205430

I. INTRODUCTION

Triggered by the spectacular rise of graphene as a unique optical and electrical material, much attention has been recently devoted to the study of other 2D atomically thin crystals [1]. Transition metal dichalcogenides such as MoS_2 possess excellent electronic and optical properties [2,3], in particular with regard to the Purcell effect and metamaterial design [4,5], while black phosphorus (BP) offers a wide tunable band gap, high carrier mobility, and large in-plane anisotropy. [6,7]. Plasmons—collective excitations of conduction electrons—are found in these materials at mid-infrared and lower frequencies when they are doped [8] or optically heated [9]. These excitations display unparalleled features that render them useful for opto-electronics. [10]. More precisely, (*i*) they are supported by a reduced number of electrons compared with other conventional plasmonic materials, such as noble metals; (*ii*) as a consequence of (*i*), a small attainable density of doping electrons is sufficient to strongly modulate their optical response; (*iii*) the atomic thickness of the material leads to a huge reduction in the plasmon wavelength and enhancement in the associated field intensity; and (*iv*) plasmons can present long lifetimes in high-quality atomically thin samples [11]. Indeed, at zero temperature and in the absence of doping, graphene, MoS_2, and BP do not support plasmons. However, these excitations are activated by introducing additional charge carriers, which can be done through chemical doping [12], molecular physisorption [13], and electrostatic gating [14,15]. The latter is useful for electrically controlling plasmons, relying, for example, on a bottom-gate configuration, as depicted in the upper inset of Fig. 1(b).

Ultrafast optical pumping also affects the electronic distribution of conduction electrons, essentially introducing electronic heat and opening new electronic transitions that enable sufficient carrier mobility to sustain plasmons [10]. The result is roughly equivalent to doping, as illustrated in Fig. 1. The ultrafast response of optically heated graphene has been probed through pump-probe spectroscopy and has been shown to sustain plasmons induced by an elevated electron temperature [9,16]. Likewise, optical heating of BP has been also demonstrated to enable plasmons in the material [17]. Optical pumping causes electrons in insulating materials to be excited across the band gap, and in graphene to be promoted from the lower to the upper Dirac cone. These hot electrons (and holes) then thermalize via carrier-carrier interactions to reach a Fermi-Dirac distribution in the conduction and valence bands within ∼10's fs, reaching attainable electronic temperatures of thousands of degrees [9,17–20], and eventually relaxing to the atomic lattice temperature, with a minor overall temperature increase due to the high heat capacity of the lattice compared with electrons. Time- and angle-resolved photoemission spectroscopy (TR-ARPES) has corroborated this picture by monitoring the formation of Fermi-Dirac distributions of electrons and holes after ∼10's fs following optical pumping [21–25]. The presence of the so-called thermoplasmons when the electronic temperature is sufficiently high has been recently corroborated in high-quality graphene through ultrafast near-field spatial imaging [9]. Plasmon switching based upon optical pumping has also been demonstrated [26], while it has been proposed that gain resulting from population inversion could compensate for losses under these circumstances [27–29].

In this paper, we analyze the plasmonic response obtained under doping and ultrafast pumping for a selection of three 2D materials: graphene, MoS_2, and BP. We study their respective plasmon dispersion relations, which evolve from low to high parallel wave vectors $\boldsymbol{q}$ until the plasmons enter the electron-hole-pair-excitation region, where they are extinguished by Landau damping. A rigorous description of these effects requires the inclusion of spatial dispersion (i.e., nonlocal

*rp@nano.aau.dk
†javier.garciadeabajo@nanophotonics.es

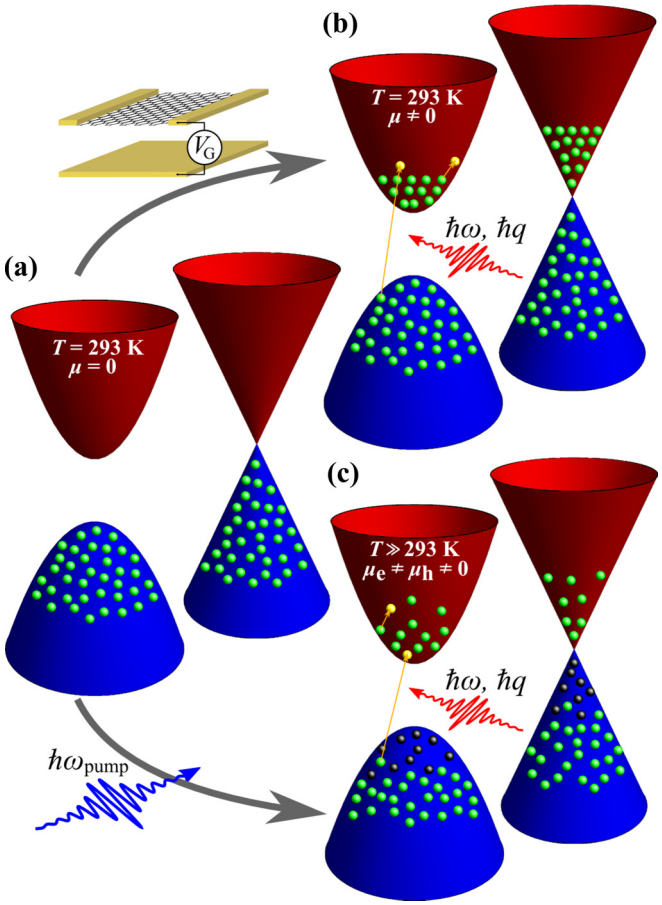

FIG. 1. Schematic band structure diagrams and electron populations in three different scenarios for parabolic semiconductor (left) and massless Dirac-fermion (right) 2D materials. (a) Undoped system at low temperature and zero doping. (b) Doped system at low temperature. (c) Optically pumped system with conduction (electrons) and valence (holes) subsystems at elevated temperatures in instantaneous thermal equilibrium, with chemical potentials μ_e and μ_h, respectively. The systems are probed with a light pulse of energy and momentum $\hbar\omega$ and $\hbar\boldsymbol{q}$.

effects, NLEs) in a realistic manner, which we achieve by adopting the random-phase approximation [30] (nonlocal-RPA) for monolayers of these three materials, using as input the single-electron wave functions obtained from a tight-binding (TB) parametrization of the valence band region [31,32]. Graphene and MoS_2 are nearly isotropic [33] in contrast to BP [15], which we explore for 2D optical wave vector $\boldsymbol{q}$ oriented along both ΓX and ΓY directions. We compare the full nonlocal-RPA response with semianalytical results obtained in the local low-$\boldsymbol{q}$ limit (local-RPA), and more precisely, we present dispersion relations under a wide range of doping and heating conditions. The effect of pumping is found to be roughly equivalent to doping, with a temperature-dependent effective Fermi energy obtained for each of the materials under consideration. We also discuss the Purcell factor, that is, the enhancement of the decay rate of an oscillating dipole in the vicinity of a nanostructured material relative to the free-space value. In particular, we study its dependence on the existence of thermally activated plasmons as a physically meaningful parameter that is highly dependent on the presence of NLEs. Our paper provides the basis for understanding and exploring the dependence of plasmons on doping and optical pumping conditions in these materials.

II. THEORETICAL FORMALISM

We use a TB model to describe each of the three materials under consideration. Graphene has been extensively studied in the literature using a two-band π-electron TB model with one orbital per carbon atom [31,34] and a hopping parameter of t, for which we adopt the value $t = 3.03$ eV [35] (it should be noted that the exact value of t varies in the literature depending on the experimental quantity that is used to fit it [36], or when based on first-principles simulations [37]). For MoS_2, we consider interactions up to third nearest neighbors, with TB parameters fitted to a generalized-gradient approximation (GGA) calculation, as reported by Liu *et al.* [32]. The parametrized bands agree well with the GGA calculation for electronic transitions in the 0–3 eV range under consideration. For BP, we use the two-band density-functional theory (DFT) TB parametrization reported in Ref. [38], which describes reasonably well the low-energy response up to 0.5 eV away from the band edges and also captures the band anisotropy. However, because it is based on DFT, it underestimates the band gap of BP. More accurate GW-Bethe-Salpeter simulations properly accounting for electron-hole interactions suggest an optical band gap of 1.2 eV [39], so we rigidly shift the conduction band upward to match this gap. The zero-point of one-electron-state energies is taken at the Dirac point in graphene and at the middle of the gap in the other two materials.

We calculate the 2D wave vector and frequency-dependent nonlocal-RPA conductivity $\sigma = \sigma' + i\sigma''$ using a well-known expression for the real part [33,40],

$$\sigma'(\boldsymbol{q},\omega) = \frac{e^2\omega}{2\pi q^2}\sum_{m,n}\int_{\mathrm{BZ}} f_{nm}^{\boldsymbol{q}}\left|M_{mn}^{\boldsymbol{q}}\right|^2\delta\left(E_{mn}^{\boldsymbol{q}} - \hbar\omega\right)d^2\boldsymbol{k}, \quad (1)$$

where $M_{mn}^{\boldsymbol{q}} = \langle\Psi_m^{\boldsymbol{k}-\boldsymbol{q}/2}|\, e^{-i\boldsymbol{q}\cdot\boldsymbol{r}}\,|\Psi_n^{\boldsymbol{k}+\boldsymbol{q}/2}\rangle$, $E_{mn}^{\boldsymbol{q}} = E_m^{\boldsymbol{k}-\boldsymbol{q}/2} - E_n^{\boldsymbol{k}+\boldsymbol{q}/2}$, $f_{nm}^{\boldsymbol{q}} = f(E_n^{\boldsymbol{k}+\boldsymbol{q}/2}) - f(E_m^{\boldsymbol{k}-\boldsymbol{q}/2})$, $f(E)$ is the Fermi-Dirac distribution, $\Psi_m^{\boldsymbol{k}}$ are Bloch wave functions of wave vector $\boldsymbol{k}$ in band m, the integral extends of the first Brillouin zone (BZ), and the sums run over band indices m and n. This is a general result that includes both inter- and intraband electronic transitions, assuming zero damping in the response. We then obtain the imaginary part σ'' using the Kramers-Krönig relations and apply a convolution with a Lorentzian to introduce a finite broadening of full-width-at-half-maximum (FWHM) $\hbar\gamma = 5$ meV. The broadening is introduced to account for a phenomenological relaxation time and to soften the unphysically strong resonances found from Eq. (1). We employ the triangle integration method [41] with $\sim 1.5 \times 10^6$ $\boldsymbol{k}$ points in the entire Brillouin zone, which is sufficient to achieve converged results. We adopt an energy grid consisting of 20,000 points logarithmically distributed in the 0–20 eV range, so that we have higher sampling density at low energies where Eq. (1) produces sharp features in the spectrum for small q (see Supplemental Material (SM) [42]).

In the $q \to 0$ limit, Eq. (1) reduces to the local-RPA conductivity. In particular, the intraband contribution (i.e., $m = n$) involves $\lim_{q\to 0} M_{nn}^{\boldsymbol{q}} = 1$, and additionally the δ function (energy conservation) allows us to replace $\hbar\omega$ by $E_{nn}^{\boldsymbol{q}}$ inside the sum. We further use the limits

$$\begin{aligned} \lim_{q\to 0} E_{nn}^{\boldsymbol{q}} &= 0, \\ \lim_{q\to 0} f_{nn}^{\boldsymbol{q}}/q &= f'(E_n)\nabla_{\boldsymbol{k}} E_n \cdot \hat{\boldsymbol{q}}, \\ \lim_{q\to 0} E_{nn}^{\boldsymbol{q}}/q &= \nabla_{\boldsymbol{k}} E_n \cdot \hat{\boldsymbol{q}}, \end{aligned} \tag{2}$$

with $\hat{\boldsymbol{q}} = \boldsymbol{q}/q$, perform the Kramers-Krönig transformation, and introduce a spectral broadening γ. The local intraband contribution thus reduces to the Drude response

$$\sigma_{\text{intra}}(\omega) = \frac{i\omega_{\text{p}}^2/4\pi}{\omega + i\gamma}, \tag{3}$$

with the plasma frequency ω_{p} given by

$$\omega_{\text{p}}^2 = \frac{-2e^2}{\pi\hbar^2} \sum_n \int_{\text{BZ}} f'(E_n)(\nabla_{\boldsymbol{k}} E_n \cdot \hat{\boldsymbol{q}})^2 \, d^2\boldsymbol{k}. \tag{4}$$

For the interband contribution, the exponential function in Eq. (1) becomes $e^{-i\boldsymbol{q}\cdot\boldsymbol{r}} \approx 1 - i\boldsymbol{q}\cdot\boldsymbol{r}$ for $q \to 0$, where the first term yields a vanishing contribution by virtue of orthogonality of the electronic states. The remaining part is proportional to q and involves $\langle \Psi_m^{\boldsymbol{k}-\boldsymbol{q}/2} | \, \boldsymbol{r} \, | \Psi_n^{\boldsymbol{k}+\boldsymbol{q}/2} \rangle = i\hbar/(m_{\text{e}} E_{mn}^{\boldsymbol{q}}) \langle \Psi_m^{\boldsymbol{k}-\boldsymbol{q}/2} | \, \boldsymbol{p} \, | \Psi_n^{\boldsymbol{k}+\boldsymbol{q}/2} \rangle = i\hbar/(m_{\text{e}} E_{mn}^{\boldsymbol{q}}) \boldsymbol{P}_{mn}^{\boldsymbol{q}}$ [43], where m_{e} is the electron mass, $\boldsymbol{p}$ is the momentum operator, and $\boldsymbol{P}_{mn}^{\boldsymbol{q}}$ is the momentum matrix element. Putting these elements together, we can write

$$\sigma'_{\text{inter}}(\omega) = \frac{e^2}{2\pi m^2 \omega} \sum_{n\neq m} \int_{\text{BZ}} f_{nm} |\hat{\boldsymbol{q}} \cdot \boldsymbol{P}_{mn}|^2 \delta\left(E_{mn}^{\boldsymbol{q}} - \hbar\omega\right) d^2\boldsymbol{k}, \tag{5}$$

where we have again made the substitution $E_{mn}^{\boldsymbol{q}} \to \hbar\omega$. Equations (3)–(5) give the local-RPA limit of the conductivity [41,44]. Note that for the photon frequencies ω under consideration, the light wave vector ω/c is small compared with the typical values of q for which plasmons are observed in 2D materials. We therefore neglect retardation effects. Additionally, we have numerically verified the convergence of the nonlocal-RPA to the local-RPA for $q \to 0$, and further found that Eq. (1) agrees with the local-RPA when describing physical quantities such as the Purcell factor, except for relatively large values of q encountered at short emitter-surface distances (see SM [42]).

We model pumping of the intrinsic materials through the Fermi-Dirac distributions f_{e} and f_{h} of hot electrons and holes at temperature T and chemical potentials μ_{e} and μ_{h}, respectively. Additionally, T is determined by the nature of the pumping process, while μ_{e} and μ_{h} must satisfy the condition that the number of electrons in the conduction band equals the number of holes in the valence band such as to maintain charge neutrality of the system, that is, $\int_{E_{\text{c}}}^{\infty} D(E) f_{\text{e}}(E) dE = \int_{-\infty}^{E_{\text{v}}} D(E) f_{\text{h}}(E) dE$, where $D(E)$ is the density of states (DOS) and E_{c} and E_{v} are the conduction and valence band edges, respectively. In graphene, the symmetry of the Dirac-cone band structure leads to $\mu_{\text{e}} = -\mu_{\text{h}}$, although this value differs from the Fermi energy (defined as the $T = 0$ limit of μ) when $\mu_{\text{e}} \ll k_{\text{B}}T$ [20]. In MoS_2 and BP, electron and hole bands are not symmetric, and interband relaxation times are considerably longer, therefore leading to different μ_{e} and $-\mu_{\text{h}}$ values. Additionally, when assuming a value of μ_{e}, we adjust μ_{h} accordingly to maintain the number of electrons in the system constant. Doping is modeled by simply increasing the chemical potential to add electrons into the system. In this case, there will be only one chemical potential, and in what follows, we use μ with no subscript to refer to the change in the Fermi energy at $T = 0$ (e.g., by gating).

III. RESULTS AND DISCUSSION

A. Plasmon dispersion

In Fig. 2, we present in the first column [Figs. 2(a)–2(c)] the band structures (left) and the DOS (right) of graphene, MoS_2, and BP, and, in columns 2 through 4 [Figs. 2(d)–2(g), 2(h)–2(k), and 2(l)–2(o)] we show the nonlocal-RPA-based loss function $\text{Im}\{r_{\text{p}}\}$, where [10]

$$r_{\text{p}} = \frac{1}{1 - i\omega/(2\pi q \sigma(\boldsymbol{q},\omega))} \tag{6}$$

is the reflection coefficient of a self-standing layer for p-polarized light, neglecting retardation effects. The results are plotted as a function of optical 2D wave vector $\boldsymbol{q}$ and frequency ω. For comparison, we present additional calculations obtained within the local-RPA model in the SM [42]. Figures 2(d)–2(g) (second column) show the response from the pristine materials (i.e., without doping and at room temperature, $T = 293$ K). Due to the absence of free charge carriers, they are incapable of supporting plasmons, so absorption comes primarily from interband transitions. For the semiconductors MoS_2 and BP, the weak absorption observed at energies below the band gap is an effect originating in electronic damping, which produces a finite conductivity even at $\omega = 0$.

Next, we investigate the effect of doping and pumping on the optical dispersion. An elevated electronic temperature produced upon optical pumping is equivalent to an increase in the effective chemical potential [10]. The equivalent μ^{eq} is such that it produces at room temperature the same Drude plasma frequency ω_{p} as for a specific pair of μ_{e} and T. We explore this equivalence in the three materials under consideration, and we expect it to hold approximately even in the nonlocal-RPA model for moderate values of q. We provide spectra in the SM [42] showing that this is a reasonable approximation. In Fig. 3, we show μ^{eq} for all three materials and for different electronic temperatures. For graphene, μ^{eq} shows two distinct regimes for low and high temperatures, already investigated in the literature [9,20]. When the temperature T becomes sufficiently high, μ^{eq} increases linearly with T as a direct consequence of the linearly increasing DOS around the K point. In graphene, $\mu^{\text{eq}} = 2\mu_{\text{e}}$ at $T = 0$ due to the linear bands and electron/hole symmetry. We emphasize that, for the pumping conditions represented by a specific choice of T, μ_e, and μ_h, the materials maintain charge neutrality, while this is not the case for electron doping.

With the doping-pumping equivalence established, we can determine equivalent plasmon dispersion relations in the

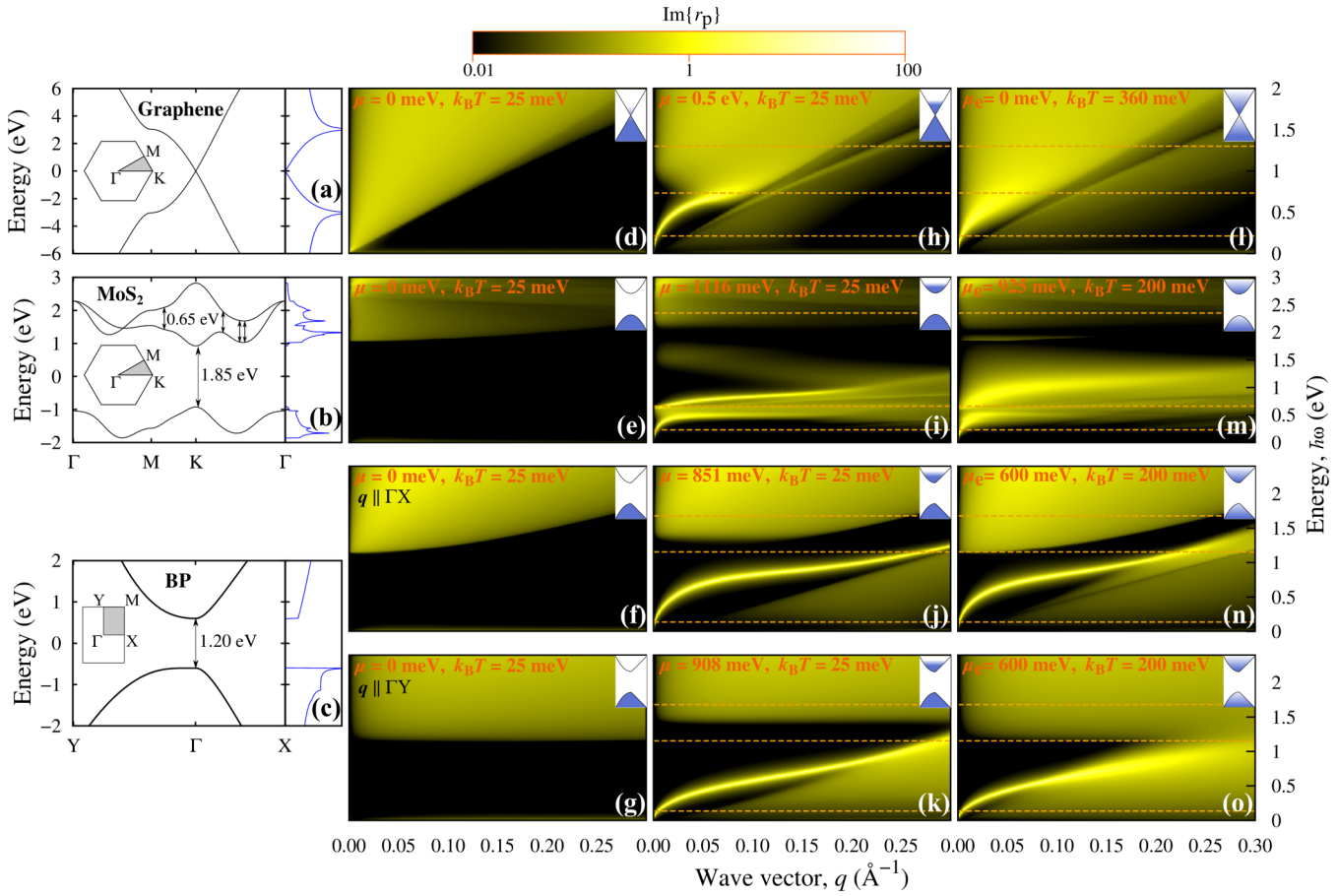

FIG. 2. (a)–(c) Band structure (left) and electronic density of states (right) for graphene, MoS_2, and BP, calculated using tight-binding models (see main text). (d)–(o) Optical dispersion diagrams calculated in the nonlocal-RPA for the selected 2D materials. For BP, we consider $\boldsymbol{q}$ oriented along either ΓX or ΓY directions. For all materials, we show the dispersion at room temperature without doping (d)–(g), at room temperature with high doping (h)–(k), and at high temperature (200 meV ≈ 2300 K) under different doping conditions (l)–(o). The chemical potential in (h)–(k) is chosen to yield a similar plasmon dispersion relation as that obtained through optical pumping at the temperatures selected in (l)–(o). The dashed lines correspond to the energies chosen for the Purcell factor calculations in Fig. 6.

doping and optical pumping schemes. In particular, we plot in the third [Figs. 2(h)–2(k)] and fourth [Figs. 2(l)–2(o)] columns of Fig. 2 the loss function Im$\{r_p\}$ for doped and heated materials, respectively. For graphene, we set $\mu_e = 0$ and choose the temperature to be equivalent to a doping of $\mu = 0.5$ eV. For the semiconductors we take $\mu_e = E_c$ to capture the longer relaxation time across the band gap and the resulting pileup of electrons and holes at the band edges, and we subsequently choose a doping level equivalent to $k_BT = 200$ meV (∼2320 K). We use these doping and temperature conditions throughout the rest of the paper, except for the BP Purcell factor calculations, in which we use the average of the band edges as μ_e.

For doped graphene, we observe the well-known plasmon dispersion relation shown in Fig. 2(h). Interband transitions are effectively suppressed at energies $\hbar\omega < 2\mu$ for $q = 0$ due to Pauli blocking, but for increasing q, this gap narrows down. With optical pumping [Fig. 2(l)], the plasmon band is clearly discernible, although it is significantly smeared out because the increased temperature produces electrons in the upper Dirac cone and holes in the lower one that enable additional intra- and interband transitions that quench the plasmons.

For doped MoS_2, we find two distinct bands: (1) a characteristic 2D plasmon starting at $\omega = 0$, made of intraband virtual transitions in the partially filled (emptied) conduction (valence) band; and (2) an optical mode starting at $\hbar\omega \approx 0.65$ eV, supported by interband transitions between the second and the third bands. We have indicated these 0.65 eV transitions in the band structure of MoS_2 shown in Fig. 2. The dispersion of both of these modes is characterized by small slopes at large wave vector $q > 0.01$ Å^{-1}. This will contribute to produce comparatively large decay rates of nearby emitters (see below). Under equivalent high temperature, these two modes are again broadened by the availability of additional intra- and interband transitions between the second and the third band. The increase of temperature additionally produces a new optical feature around ∼1.9 eV, associated with transitions between the first and second bands and enabled by partial thermal population.

For BP, the similarity between the optical modes enabled by either doping or optical pumping is striking, especially at large q. In contrast to both graphene and MoS_2, no significant band broadening is observed in the heated material because we have only two electronic bands separated by a gap of

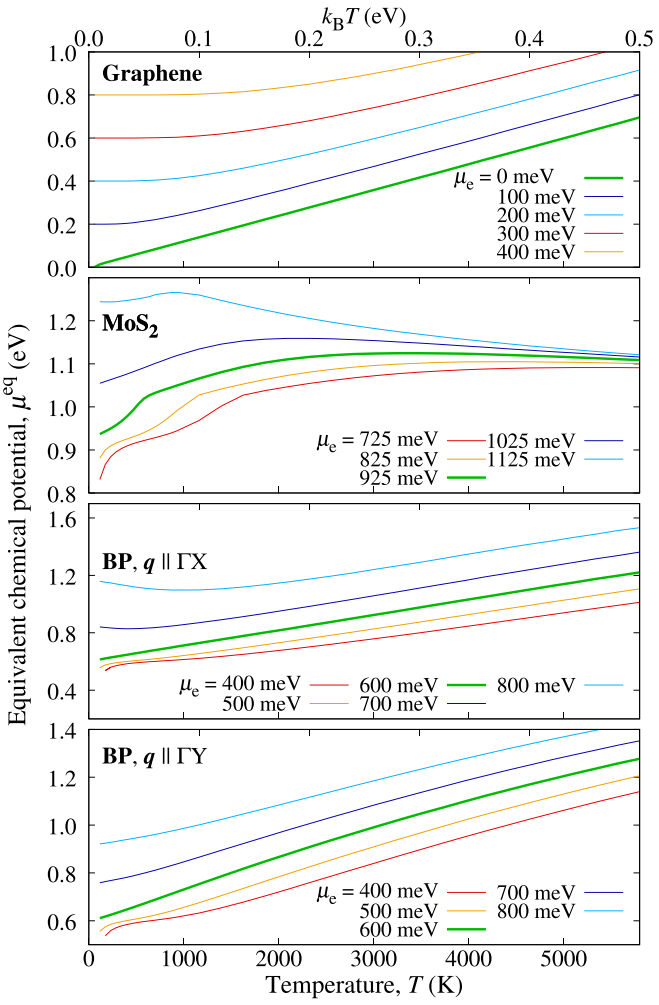

FIG. 3. Chemical potential μ^{eq} required to obtain a plasmon dispersion relation at room temperature equivalent to that observed as a function of temperature T for several fixed values of the electron chemical potential μ_e (see labels). Results for $\mu_e = E_c$ (the conduction band edge) are shown as green thick curves in all four panels. All results are obtained within the local-RPA approximation.

1.2 eV. From DFT calculations of the band structure in BP [38], we can anticipate that inclusion of more bands should also produce broadening of the plasmon resonance at elevated electron temperature. The difference between the two orientations of BP due to crystal anisotropy is clear, with two different plasmon bands that share in common the dispersion dependence $\omega \propto \sqrt{q}$ characteristic of 2D systems, in agreement with previous calculations [45].

We conclude that thermally activated plasmon modes resemble those enabled by doping, but we emphasize the transient character of the former, which can be sustained during times scales of 100's fs, because relaxation of electronic heat to phonon modes takes place. The temporal evolution dictated by relaxation should introduce an additional mechanism of plasmon broadening, which we estimate to be small compared with the intrinsic damping here assumed.

B. Purcell enhancement

We now turn to the enhancement of the decay rate of an oscillating dipole in close proximity to the materials to investigate the equivalence between doping and pumping and the coupling between plasmons in the materials and point emitters. The Purcell enhancement factor is influenced by the reflection coefficient at large q, and so it serves as an excellent probe of the importance of NLEs. For a dipole oriented parallel to the surface, the Purcell enhancement factor is given by [46,47]

$$\frac{\Gamma}{\Gamma_0} = 1 + \frac{3c^3}{4\omega^3}\int_0^\infty q^2\,\mathrm{Im}\{r_p(q,\omega)\}e^{-2qd}dq, \qquad (7)$$

where Γ_0 is the decay rate in vacuum, Γ is the decay rate in the presence of the 2D material, and d is the distance between the surface and the emitting dipole. We are working in the electrostatic limit ($\sqrt{\omega^2/c^2 - q^2} \approx iq$), which is a good approximation for the small distance $d \ll c/\omega$ under consideration, and further simplifies the numerical simulations. We note that Eq. (7) is only valid for materials in which the reflection coefficient r_p is independent of the orientation of $\boldsymbol{q}$. This is not the case of BP, for which one should carry out the corresponding azimuthal integral taking into account the full $\boldsymbol{q}$-dependence of r_p. Instead, for simplicity, we estimate the Purcell factor in BP by carrying out only the radial integral over q and averaging r_p along the ΓX and ΓY directions.

In Fig. 4, we plot the imaginary part of the reflection coefficient calculated using either the local-RPA or the nonlocal-

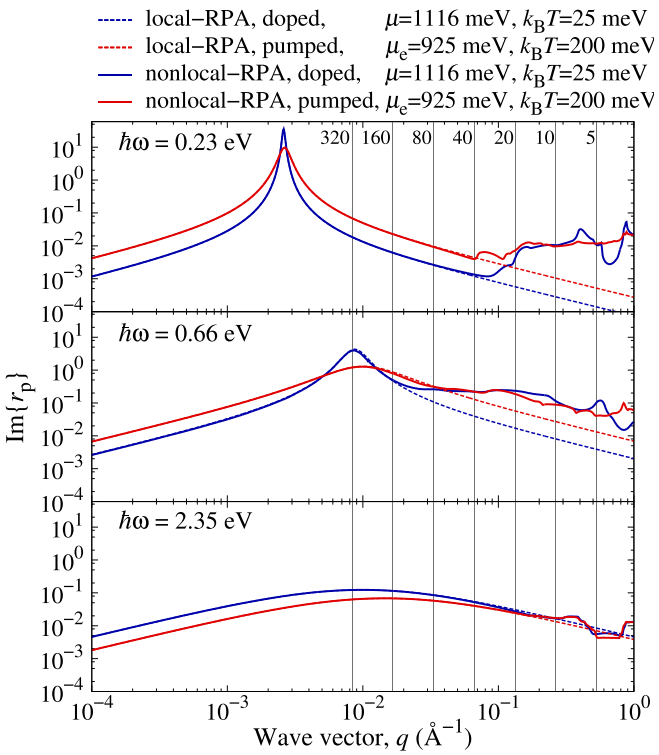

FIG. 4. Imaginary part of the Fresnel reflection coefficient for p-polarization r_p as obtained in the local-RPA (dashed curves) and the nonlocal-RPA (solid curves) for a MoS_2 atomic monolayer. We compare results with either doping and heating (red curves, $\mu_e = 925$ meV, $k_B = 200$ meV) or only doping (blue curves, $\mu = 1116$ meV, room temperature). Vertical lines mark the integration limit q_{cut} that accounts for 90% of the Purcell factor at various dipole-surface distances (top labels in Å, see text).

RPA models for MoS_2 at three different photon energies. The prominent peak observed for $\hbar\omega = 0.23$ eV is due to the excitation of plasmons, while for $\hbar\omega = 0.66$ eV the peak is due to interband absorption, as discussed above. For large q, we have $\mathrm{Im}\{r_p\} \approx q^{-1}$ in the local-RPA, just as observed in Fig. 4. In contrast, in the nonlocal-RPA σ depends on q in a more involved manner, as it reflects the details of the electronic band structure. From Fig. 4 we conclude that NLEs are not important for small values of q, but for sufficiently large q significant variations are introduced in the nonlocal reflectivity, including strong modulations and fine structure in r_p for MoS_2. Defining q_{cut} by $0.9 = \int_{\omega/c}^{q_{cut}} q^2 e^{-2qd} dq / \int_{\omega/c}^{\infty} q^2 e^{-2qd} dq$ [i.e., the upper wave vector integration limit that yields 90% of the contribution to the Purcell factor in Eq. (7)], we argue that higher q's play a marginal role, so they can be ignored. We show in Fig. 4 (vertical lines) the values of q_{cut} for a number of different values of d. For example, for $d = 40$ Å, the integral in Eq. (7) should run up to the line marked 40 Å to account for 90% of the Purcell factor. It is clear that the importance of NLEs is strongly dependent on photon energy. For 2.35 eV, significant differences are observed only for q larger than ~ 0.2 Å^{-1}, while at an energy of 0.66 eV large differences are observed already at $q \approx 0.02$ Å^{-1}. In agreement with the conclusions extracted above from the analysis of the plasmon dispersion, we find that optical pumping (i.e., heating to an equivalent high temperature) gives rise to additional broadening compared to doping, but the plasmon peak positions are almost unchanged.

In Fig. 5, we show the Purcell enhancement factor as a function of photon energy for a dipole placed parallel at a distance of 1 nm from a single atomic layer for all three materials in the local and nonlocal-RPA models under either doping or optically pumping conditions. For the doped materials, we observe a strong overall enhancement of the decay rate due to the presence of the materials. At some energies, we see a particularly strong enhancement and this is associated with the excitation of plasmons. Energy transferred during decay is then mainly deposited in the surface modes of the system, which ultimately decay into electron-hole pair transitions and finally relax to produce heating of the materials. In the local-RPA, the plasmon modes may be practically nondispersive for large q (see SM [42]), leading to artificially stronger peaks in the Purcell enhancement at these energies. In the nonlocal-RPA, however, the plasmon energy evolves with q (see Fig. 2), and thus, the enhancement is weaker and we generally observe smaller peak-to-valley ratios. Specifically for graphene, we observe a huge reduction from a ratio of ~ 25 to ~ 2, stressing that NLEs play an important role. For energies below ~ 0.4 eV, the nonlocal-RPA Purcell factor is always much larger than in the local-RPA because at $q > 0$ the intraband absorption is peaked at some energy larger than 0, in contrast to the Drude response, which produces higher losses in the low-energy regime.

The response of optically pumped graphene and MoS_2 is affected by the increase in losses due to new opened intra- and interband transition channels, which end up in an overall increase in the Purcell factor compared to doping, except at frequencies where the coupling to plasmons is strong (i.e., optical pumping reduces the peak strength of the plasmons, but creates additional decay channels to electron-hole pair transitions).

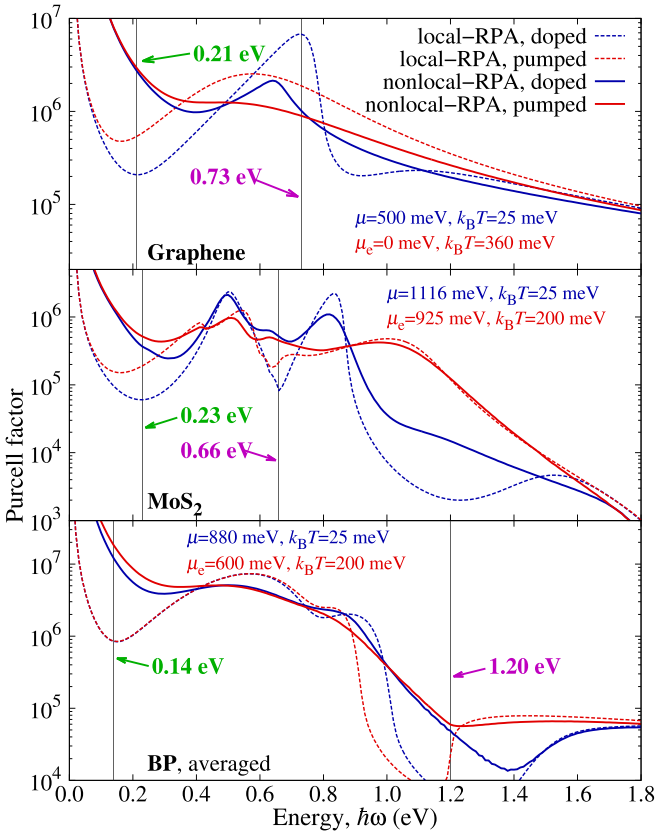

FIG. 5. Spectral dependence of the Purcell factor for a dipole emitter oriented perpendicularly to the surface and placed at a distance of 1 nm from monoatomic graphene, MoS_2, and BP layers. For BP, we present an average of the Purcell factor for the two independent directions considered in Fig. 2 (see discussion in text). We compare local-RPA (dashed curves) and nonlocal-RPA (solid curves) calculations for the material either at room temperature and high doping (blue curves) or at high temperature (red curves).

Surprisingly, in MoS_2, we observe a significant peak-to-valley ratio of approximately 5 for the 0.5 eV peak in the nonlocal-RPA calculation with optical pumping, thus suggesting that this effect may indeed be observable in a pump-probe experiment. In graphene, under the chosen high-temperature conditions, the peak vanishes entirely in the nonlocal-RPA simulations, and thus, it appears to be experimentally difficult to observe. The difference between doping and optical pumping is generally less pronounced in the nonlocal-RPA compared to the local-RPA. At low energies, this occurs because the intraband response becomes increasingly weaker for increasing q, such that the difference between doping and optical pumping does not persist in the entire integration range in Eq. (7). For high energies, it is difficult to single out a general explanation, except that increasing q in the nonlocal-RPA model may cause spectral features comparable to those obtained by increasing the temperature, something that is particularly pronounced for graphene (see Fig. S4 in the SM [42]).

In BP, broadening effects due to optical pumping are negligible at energies below the band gap in the local-RPA model because in this energy regime the only effect of increasing the temperature is to increase the plasma frequency. However, in the nonlocal-RPA calculations, we observe a

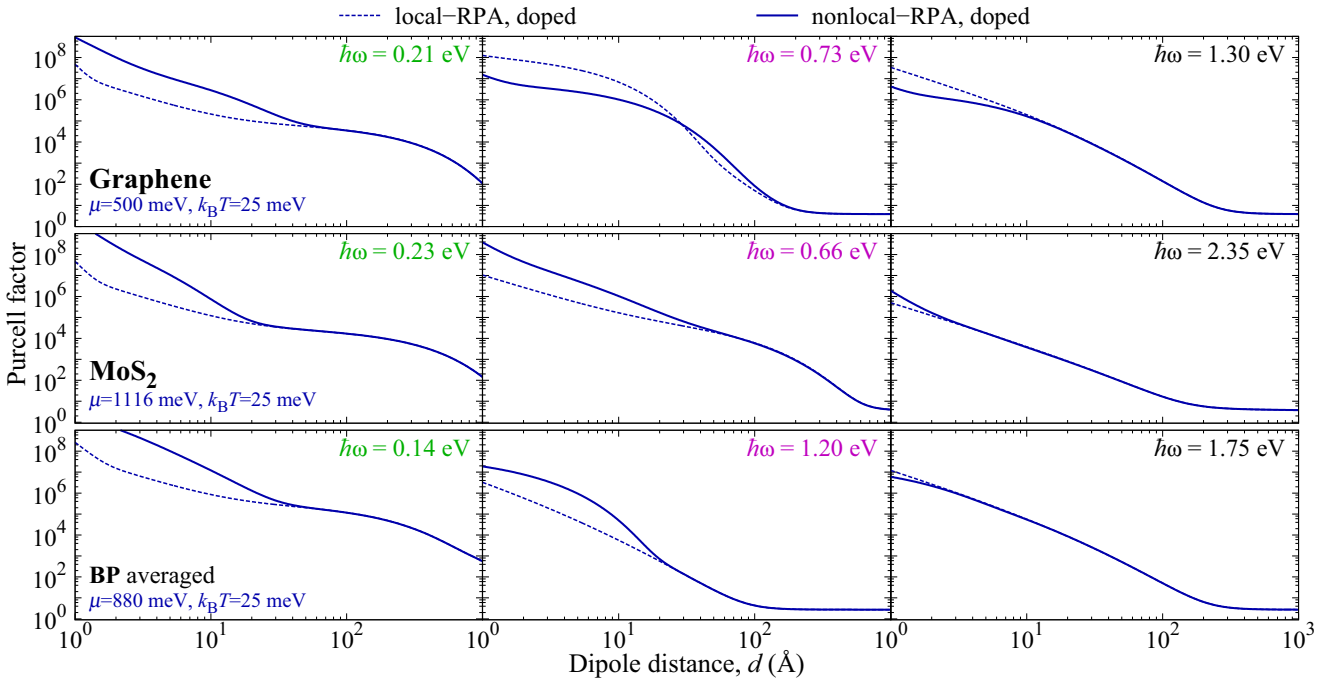

FIG. 6. Emitter-surface distance dependence of nonlocal effects in the Purcell factor. We compare local-RPA and nonlocal-RPA calculations with three different photon emission energies, chosen at the valley and peak values of the Purcell factor marked by arrows in Fig. 5, as well as at an energy in which interband transitions are the dominant contribution to absorption for each of the materials under consideration.

weak broadening because the increased temperature affects the intraband transitions at high q.

In Fig. 6, we show the dependence of the Purcell factor on the distance between the dipole and the surface for three energies corresponding to the horizontal dashed lines in Figs. 2(h)–2(o) and the vertical lines in Fig. 5. The first two energies are somewhat arbitrarily chosen at positions, for which Fig. 5 exhibits a large difference between local- and nonlocal-RPA simulations, while the highest energy lies 300 meV above the onset of interband absorption. Major deviations between the local-RPA and the nonlocal-RPA calculations are observed primarily at distances below 5 nm, although for graphene at 0.73 eV, NLEs are noticeable even up to $d = 20$ nm. For energies at which interband transitions are the major contribution to optical absorption, the correspondence between local- and nonlocal-RPA models is generally quite good. This shows that it is the intraband transitions that are most heavily influenced by NLEs. Specifically for MoS_2, we find that, moving from left to right in Fig. 6, dipole-surface distances of 2 nm, 5 nm, and 0.4 nm are the approximate locations at which NLEs become important, in good agreement with the values of q_{cut} discussed in connection with Fig. 4.

IV. CONCLUSION

We have investigated plasmons activated by either electron doping or optical pumping and their role in the enhancement of the Purcell factor for a dipole in the vicinity of one of the three 2D materials graphene, MoS_2, or BP. To treat doping and optical pumping in a comparable manner, we have calculated the equivalent doping level that produces a Drude plasmon weight similar to that obtained for a given temperature increase without doping, and we have determined plasmon dispersions and Purcell enhancement factors under these comparable conditions. The Purcell factor is highly dependent on the evanescent wave components of high spatial wave vector, and so we have adopted the nonlocal-RPA model to realistically describe the material response, and compared it with the local approximation.

We find that optical pumping (i.e., for an equivalent elevated temperature) and doping give rise to similar features in the Purcell factor, but that the former introduces extra broadening due to the opening of additional electron-hole pair transition channels that quench the plasmons. Surprisingly, for MoS_2, we find significantly high peaks in the Purcell enhancement factor, even under optical pumping conditions, indicating that it may be possible to observe a broadband Purcell enhancement experimentally in pumped MoS_2.

Under doping at low temperature, graphene exhibits large Purcell enhancement factors, which are, however, strongly reduced under equivalent high temperature with low doping conditions, due to the noted new plasmon-quenching channels. Compared with MoS_2, the optically induced increase of the Purcell factor should be difficult to observe in graphene.

We find that nonlocal effects can be generally disregarded for dipole-surface distances above ∼5 nm. However, for smaller distances, these effects can change the Purcell factor by orders of magnitude, produce smearing of spectral features in the Purcell factor, and result in generally smaller peak-to-valley ratios in the spectral dependence of this quantity.

ACKNOWLEDGMENTS

This paper has been supported in part by the Center for Nanostructured Graphene (Grant No. DNRF103, Danish National Research Foundation), the Villum Foundation

(QUSCOPE Project), the Spanish MINECO (MAT2014-59096-P, and SEV2015-0522) AGAUR (2014 SGR 1400), Fundació Privada Cellex, and the European Commission (Graphene Flagship 696656).

[1] D. N. Basov, M. M. Fogler, and F. J. García de Abajo, Science **354**, aag1992 (2016).
[2] K. F. Mak and J. Shan, Nat. Photon. **10**, 216 (2016).
[3] Y. Venkata Subbaiah, K. Saji, and A. Tiwari, Adv. Funct. Mater. **26**, 2046 (2016).
[4] M. N. Gjerding, M. Pandey, and K. S. Thygesen, Nat. Commun. **8**, 15133 (2017).
[5] M. N. Gjerding, R. Petersen, T. G. Pedersen, N. A. Mortensen, and K. S. Thygesen, Nat. Commun. **8**, 320 (2017).
[6] F. Xia, H. Wang, and Y. Jia, Nat. Commun. **5**, 4458 (2014).
[7] X. Ling, H. Wang, S. Huang, F. Xia, and M. S. Dresselhaus, Proc. Natl. Acad. Sci. USA **112**, 4523 (2015).
[8] J. Chen, M. Badioli, P. Alonso-González, S. Thongrattanasiri, F. Huth, J. Osmond, M. Spasenović, A. Centeno, A. Pesquera, P. Godignon, A. Zurutuza Elorza, N. Camara, F. J. García de Abajo, R. Hillenbrand, and F. H. L. Koppens, Nature **487**, 77 (2012).
[9] M. Wagner, A. S. McLeod, S. J. Maddox, Z. Fei, M. Liu, R. D. Averitt, M. M. Fogler, S. R. Bank, F. Keilmann, and D. Basov, Nano Lett. **14**, 4529 (2014).
[10] F. J. García de Abajo, ACS Photon. **1**, 135 (2014).
[11] A. Woessner, M. B. Lundeberg, Y. Gao, A. Principi, P. Alonso-González, M. Carrega, K. Watanabe, T. Taniguchi, G. Vignale, M. Polini, J. Hone, R. Hillenbrand, and F. H. Koppens, Nat. Mater. **14**, 421 (2015).
[12] Y. Wang, J. Z. Ou, A. F. Chrimes, B. J. Carey, T. Daeneke, M. M. Alsaif, M. Mortazavi, S. Zhuiykov, N. Medhekar, M. Bhaskaran *et al.*, Nano Lett. **15**, 883 (2015).
[13] S. Tongay, J. Zhou, C. Ataca, J. Liu, J. S. Kang, T. S. Matthews, L. You, J. Li, J. C. Grossman, and J. Wu, Nano Lett. **13**, 2831 (2013).
[14] C.-P. Lu, G. Li, J. Mao, L.-M. Wang, and E. Y. Andrei, Nano Lett. **14**, 4628 (2014).
[15] T. Low, R. Roldán, H. Wang, F. Xia, P. Avouris, L. M. Moreno, and F. Guinea, Phys. Rev. Lett. **113**, 106802 (2014).
[16] M. Wagner, Z. Fei, A. S. McLeod, A. S. Rodin, W. Bao, E. G. Iwinski, Z. Zhao, M. Goldflam, M. Liu, G. Dominguez *et al.*, Nano Lett. **14**, 894 (2014).
[17] M. A. Huber, F. Mooshammer, M. Plankl, L. Viti, F. Sandner, L. Z. Kastner, T. Frank, J. Fabian, M. S. Vitiello, T. L. Cocker *et al.*, Nat. Nanotech. **12**, 207 (2017).
[18] A. Grubisic Cabo, J. A. Miwa, S. S. Grønborg, J. M. Riley, J. C. Johannsen, C. Cacho, O. Alexander, R. T. Chapman, E. Springate, M. Grioni *et al.*, Nano Lett. **15**, 5883 (2015).
[19] H. Wang, C. Zhang, and F. Rana, Nano Lett. **15**, 339 (2014).
[20] R. Yu, A. Manjavacas, and F. J. García de Abajo, Nat. Commun. **8**, 2 (2017).
[21] S. Ulstrup, J. C. Johannsen, M. Grioni, and P. Hofmann, Rev. Sci. Instrum. **85**, 013907 (2014).
[22] S. Ulstrup, J. C. Johannsen, F. Cilento, A. Crepaldi, J. A. Miwa, M. Zacchigna, C. Cacho, R. T. Chapman, E. Springate, F. Fromm *et al.*, J. Electron. Spectrosc. Relat. Phenom. **200**, 340 (2015).
[23] M. Breusing, C. Ropers, and T. Elsaesser, Phys. Rev. Lett. **102**, 086809 (2009).
[24] J. C. Johannsen, S. Ulstrup, F. Cilento, A. Crepaldi, M. Zacchigna, C. Cacho, I. E. Turcu, E. Springate, F. Fromm, C. Raidel *et al.*, Phys. Rev. Lett. **111**, 027403 (2013).
[25] J. C. Johannsen, S. Ulstrup, A. Crepaldi, F. Cilento, M. Zacchigna, J. A. Miwa, C. Cacho, R. T. Chapman, E. Springate, F. Fromm *et al.*, Nano Lett. **15**, 326 (2014).
[26] G. Ni, L. Wang, M. Goldflam, M. Wagner, Z. Fei, A. McLeod, M. Liu, F. Keilmann, B. Özyilmaz, A. C. Neto *et al.*, Nat. Photon. **10**, 244 (2016).
[27] O. Hess, J. B. Pendry, S. A. Maier, R. F. Oulton, J. Hamm, and K. Tsakmakidis, Nat. Mater. **11**, 573 (2012).
[28] F. Rana, IEEE Trans. Nanotechnol. **7**, 91 (2008).
[29] Z. Sun, D. N. Basov, and M. M. Fogler, Phys. Rev. Lett. **117**, 076805 (2016).
[30] D. Pines and P. Nozières, *The Theory of Quantum Liquids* (W. A. Benjamin, Inc., New York, 1966).
[31] A. H. Castro Neto, F. Guinea, N. M. R. Peres, K. S. Novoselov, and A. K. Geim, Rev. Mod. Phys. **81**, 109 (2009).
[32] G.-B. Liu, W.-Y. Shan, Y. Yao, W. Yao, and D. Xiao, Phys. Rev. B **88**, 085433 (2013).
[33] A. Hill, S. Mikhailov, and K. Ziegler, Europhys. Lett. **87**, 27005 (2009).
[34] P. R. Wallace, Phys. Rev. **71**, 622 (1947).
[35] R. Saito, G. Dresselhaus, and M. S. Dresselhaus, *Physical Properties of Carbon Nanotubes* (World Scientific, London, 1998), Vol. 35.
[36] A. Bostwick, T. Ohta, T. Seyller, K. Horn, and E. Rotenberg, Nat. Phys. **3**, 36 (2007).
[37] P. E. Trevisanutto, C. Giorgetti, L. Reining, M. Ladisa, and V. Olevano, Phys. Rev. Lett. **101**, 226405 (2008).
[38] A. S. Rodin, A. Carvalho, and A. H. Castro Neto, Phys. Rev. Lett. **112**, 176801 (2014).
[39] V. Tran, R. Soklaski, Y. Liang, and L. Yang, Phys. Rev. B **89**, 235319 (2014).
[40] H. Ehrenreich and M. H. Cohen, Phys. Rev. **115**, 786 (1959).
[41] T. G. Pedersen, C. Flindt, J. Pedersen, A.-P. Jauho, N. A. Mortensen, and K. Pedersen, Phys. Rev. B **77**, 245431 (2008).
[42] See Supplemental Material at http://link.aps.org/supplemental/10.1103/PhysRevB.96.205430 for more details of the theoretical formalism.
[43] L. C. Lew Yan Voon and L. R. Ram-Mohan, Phys. Rev. B **47**, 15500 (1993).
[44] T. G. Pedersen, P. Modak, K. Pedersen, N. E. Christensen, M. M. Kjeldsen, and A. N. Larsen, J. Phys.: Condens. Matter **21**, 115502 (2009).
[45] F. Jin, R. Roldán, M. I. Katsnelson, and S. Yuan, Phys. Rev. B **92**, 115440 (2015).
[46] F. H. L. Koppens, D. E. Chang, and F. J. García de Abajo, Nano Lett. **11**, 3370 (2011).
[47] L. Novotny and B. Hecht, *Principles of Nano-Optics* (Cambridge University Press, New York, 2006).